# Smart Artificial Soft Tissue - Application to a Hybrid Simulator for Training of Laryngeal Pacemaker Implantation

Thomas Thurner, Benjamin Esterer, David Fürst, Marianne Hollensteiner, *Member, IEEE*, Sabrina Sandriesser, Peter Augat, Roland Pruckner, Daniela Wirthl, Martin Kaltenbrunner, Andreas Müller, Gerhard Förster, Claus Pototschnig, and Andreas Schrempf

***Abstract*—Surgical simulators are safe and evolving educational tools for developing surgical skills. In particular, virtual and hybrid simulators are preferred due to their detailedness, customization and evaluation capabilities. To accelerate the revolution of a novel class of hybrid simulators, a Smart Artificial Soft Tissue is presented here, that determines the relative position of conductive surgical instruments in artificial soft tissue by inverse resistance mappings without the need for a fixed reference point. This is particularly beneficial for highly deformable structures when specific target regions need to be reached or avoided. The carbon-black-silicone composite used can be shaped almost arbitrarily and its elasticity can be tuned by modifying the silicone base material. Thus, objective positional feedback for haptically correct artificial soft tissue can be ensured. This is demonstrated by the development of a laryngeal phantom to simulate the implantation of laryngeal pacemaker electrodes. Apart from the position-detecting larynx phantom, the simulator uses a tablet computer for the virtual representation of the vocal folds' movements, in accordance with the electrical stimulation by the inserted electrodes. The possibility of displaying additional information about target regions and anatomy is intended to optimize the learning progress and illustrates the extensibility of hybrid surgical simulators.**

***Index Terms*—Artificial tissue, hybrid medical simulation, laryngeal pacemaker, electrode positioning, haptical realistic, soft sensor, position detection.**

Manuscript received 24 February 2022; revised 27 July 2022; accepted 21 August 2022. Date of publication 25 August 2022; date of current version 20 January 2023. This work was supported in part by the Austrian Research Promotion Agency (FFG) Project under Grant 845436 and in part by the Company MED-EL Elektromedizinische Geräte Gesellschaft m.b.H., Innsbruck, Austria. *(Corresponding author: Thomas Thurner.)*

Thomas Thurner is with the Research Group for Surgical Simulators Linz, Upper Austria University of Applied Sciences, 4020 Linz, Austria, and also with the Division of Soft Matter Physics, Institute for Experimental Physics, Johannes Kepler University, 4040 Linz, Austria (e-mail: thomas.thurner@fh-linz.at).

Benjamin Esterer is with the Research Group for Surgical Simulators Linz, Upper Austria University of Applied Sciences, Austria, and also with the Institute for Biomechanics, Berufsgenossenschaftliche Unfallklinik Murnau and Paracelsus Medical University Salzburg, Germany.

David Fürst is with the Department of Acoustic Engineering, GE Healthcare Austria GmbH & Co OG, Austria.

Marianne Hollensteiner, Sabrina Sandriesser, and Peter Augat are with the Institute for Biomechanics, Berufsgenossenschaftliche Unfallklinik Murnau and Paracelsus Medical University Salzburg, Germany.

Roland Pruckner and Martin Kaltenbrunner are with the Division of Soft Matter Physics, Institute for Experimental Physics, Johannes Kepler University, Austria, and also with the Soft Materials Lab, Linz Institute of Technology, Johannes Kepler University, Austria.

Daniela Wirthl is with the Division of Soft Matter Physics, Institute for Experimental Physics, Johannes Kepler University, Austria.

Andreas Müller and Gerhard Förster are with the Otorhinolaryngology, SRH Wald-Klinikum, Germany.

Claus Pototschnig is with the Otorhinolaryngology, Innsbruck University Hospital, Austria.

Andreas Schrempf is with the Research Group for Surgical Simulators Linz, Upper Austria University of Applied Sciences, Austria.

This article has supplementary downloadable material available at https://doi.org/10.1109/TBME.2022.3201613, provided by the authors.

Digital Object Identifier 10.1109/TBME.2022.3201613

## I. Introduction

SURGICAL simulation has proven to be an essential training method to significantly improve skills, especially of young physicians, or when practicing innovative new surgical approaches without risk to patients [1], [2]. As a result of constantly advancing research, various types of simulators have been developed that can simulate increasingly complex processes [3]. A rough distinction can be made between four categories: simulation using animal trials, experiments on human cadavers, simulations with synthetic replicas of anatomies, and electronically enhanced or visual replicas [4]. The latter category also includes virtual reality (VR)-based simulators and hybrid simulators that combine different technologies to optimize training. Many new simulators belong to the latter group [1], [5], [6], [7], [8], [9].

Despite all advantages of purely visual simulators, haptic components often remain indispensable [5]. In particular, instrument handling and the haptic perception of different tissue layers during cutting or penetration represents a critical core competence. The aim of a hybrid simulator is therefore to seamlessly combine animations and evaluations of virtual simulators [6], [10] including their level of detail, with realistic haptic components of passive simulators [11], [12], [13]. Also, the chance of using real surgical instruments with all their capabilities should be taken. Such a combination of different systems can deliver good results in terms of learning success, as already shown in first publications [7], [8], [14], [15].

Typically optical or electromagnetic systems are used for instrument tracking. In optical tracking systems, visual markers are placed on the instruments and the patient phantom.

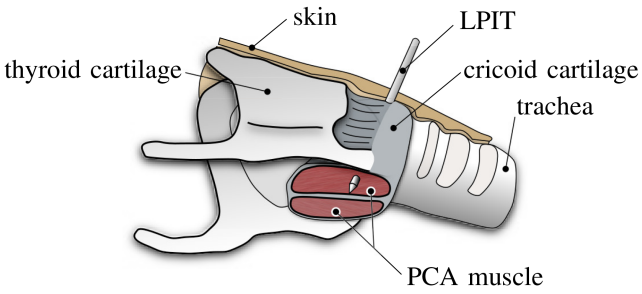


Fig. 1. Anatomy of the larynx showing PCA muscle and LPIT.

Their positions are captured by cameras and the position and orientation of the instrument relative to the camera system is determined [16], [17]. This position data can be embedded in virtual animations. Especially when interacting with artificial soft tissue, representing muscles or connective tissue, optical systems fail to provide accurate results, since in most cases the markers cannot be placed directly on or inside the deformable phantom parts. Electromagnetic tracking systems, on the other hand, obtain the position and orientation of small target coils within a generated magnetic field [18], where these small coils can be directly applied to the deformable artificial tissue. However, the coils are expensive, alter the haptics of soft tissue and require a cable connection between each coil and the tracking system, which limits their usage in hybrid simulators. In addition, this technique brings limitations to the use of metals in the detection area, as they affect the electromagnetic field and thus the tracking accuracy.

This work describes a cost-effective alternative to complex tracking systems, the development of "Smart Artificial Soft Tissue," tissue-mimicking patient phantom parts which provide realistic haptic feedback and integrated sensing capabilities. The objective is to develop an intelligent artificial human larynx that focuses on the cricoid region and posterior cricoarytenoid muscles to provide a realistic training environment for the most critical part during the implantation of a laryngeal pacemaker (LP) system (MED-EL Elektromedizinische Geräte Gesellschaft m.b.H., Innsbruck, Austria).

Apart from preclinical evaluation of the LP system [19], functional testing is also usually performed on animals to evaluate the evoked responses to electrical stimulation. Not only ethical concerns might arise from animal testing but also high costs might be associated. Considering the 3R principle for replacement, refinement and reduction in preclinical testing, using a simulator for training purposes is even more preferable.

Such a surgical simulator needs to meet specific requirements to be a real alternative. Haptic perception when advancing an LP Insertion Tool (LPIT) through different soft tissue layers such as skin, mucosa, cartilage and muscle tissue is a key skill to learn (Fig. 1). The correct positioning of the electrode into the posterior cricoarytenoid (PCA) muscle ultimately determines whether the vocal fold can be opened correctly by neuromuscular stimulation. For this purpose, it is essential to determine instrument position on deformable phantom parts. The hybrid simulator to be presented aims to include an artificial larynx with different, haptically realistic tissue layers and an artificial PCA muscle realized as Smart Artificial Soft Tissue. To achieve the key learning objectives, the focus will be on the fusion of position recognition and haptic realism in a hybrid environment.

## II. Material and Methods

### A. Laryngeal Pacemaker and Electrode Implantation

The LP System [20] was developed by MED-EL to treat patients with bilateral vocal fold paralysis and is based on the concept of selective neurostimulation of terminal abductor branches of the recurrent laryngeal nerve (RLN) [21]. The LP-System requires to find a sensitive area, a so-called hotspot, on the PCA muscle in order to control the opening of the vocal fold. During implantation, hotspot identification and electrode fixation are the most critical steps and hence are thought to be most beneficial to train in a hybrid simulator. To target the hotspot, the LPIT is used to allow a minimally invasive electrode placement into the PCA. The LPIT is a bipolar electrode consisting of a trocar and a canula. After a small horizontal skin incision over the cricoid, the LPIT is advanced across the upper border of the cricoid arch and pushed submucosally along the inner surface of the arch towards the cricoid lamina. Penetrating the lamina requires advancing the LPIT gradually and gently, applying slight rotary movements, until the PCA muscle is reached and a hotspot hopefully found (Fig. 1). For verification, electrical stimulation is used under videolaryngoscopic monitoring of the vocal fold movements [20]. If necessary, the LPIT position can be changed by retracting it from the lamina, repositioning it, and advancing it again until the hotspot (with the best abduction of the vocal fold) is found in the PCA.

### B. Haptically Realistic Artificial Tissue

***1) Tissue Development:*** The challenge of developing an artificial larynx with a cricoid cartilage lies in the interaction of materials of different hardness and toughness. Therefore, the haptically realistic design has only been created for those structures that are actually relevant during surgical simulation or need to be penetrated by the LPIT. Here, these are the outer skin, the cartilage itself and the tissue directly surrounding it.

The development of the artificial cricoid was based on expert opinions and material tests. First, the outer shell of the cricoid cartilage was 3D printed using Ultimaker TPU95 A (Ultimaker B.V., Utrecht, The Netherlands) filament. The print had a general wall thickness of 1 mm and a layer height of 0.1 mm without any filling. Only the wall thickness on the side facing the injection site was reduced to 0.3 mm by decreasing the number of 3D-printed layers. In addition, the same side was covered with a thin layer (0.2 mm) of super glue (Loctite Super Glue Liquid, Henkel AG & Co. KGaA, Düsseldorf, Germany) to generate a small, sharp first insertion force peak. This empty shell was filled with an urethane rubber (PMC780 from Smooth-On, Inc., Macungie, PA, USA) mixed with silicone oil (AP100 from Wacker Chemie AG, München, Germany) at a ratio of 30:9 by weight to reduce the friction of the LPIT while sliding through the urethane rubber. To ensure a better connection between soft tissue and

(a) (b)

Fig. 2. Cricoid cartilage and surrounding tissue - real cricoid of a human versus artificial, simplified replica; (a) measuring forces while penetrating cricoid cartilage, (b) rendering of an artificial, simplified cricoid cartilage (white) with soft tissue (pink) and sensor mat ("Smart Artificial Soft Tissue," black) underneath (soft tissue partially removed to reveal cartilage).

cartilage, polyester wadding was glued to the inner surface of the cricoid with silicone glue (Sil-Poxy from Smooth-On, Inc., Macungie, PA, USA). Similar to other simulators [22], [23], the soft tissue around the cartilage was casted with silicone (Ecoflex 0030 from Smooth-On, Inc., Macungie, PA, USA) (Fig. 2(b)).

The skin covering the larynx is made of DRAGON SKIN 20 with embedded POWER MESH (both from Smooth-On, Inc., Macungie, PA, USA). This mesh serves to increase the tear resistance of the silicone when it is spread, making the skin more durable.

***2) Animal and Human Specimens:*** In order to evaluate the haptic requirements of an artificial cricoid cartilage, the core of the physical haptic simulator, the forces applied to the LPIT during penetration were measured. For this purpose, porcine and human specimens were used as references.

Ten larynges of 180-day-old pigs (sex unknown) provided by a farmer (Schickmair Florian, Schickmair Ab-Hof-Vermarktung KG, Gunskirchen, Austria) served as reference structures (byproduct of meat processing). The porcine samples were tested in accordance with the Austrian Federal Act on Hygiene Requirements for Animal By-products and Materials Not Intended for Human Consumption (Tiermaterialiengesetz – TMG, BGBl. I Nr. 141/2003) at the University of Applied Sciences Upper Austria (Linz, Austria). The larynges were prepared and measured within 24 hours after slaughter (storage $<4\,^{\circ}$C, packed airtight). For the measurement, the surrounding soft tissue was removed and only the cricoid cartilage itself was measured. Due to deviations or damages during preparation, only 6 of them were actually measured. The specimens were fixed by casting the cricoid anterior arch with urethane casting resin (Smooth-cast 65D, Smooth-On, Inc., Macungie, PA, USA), taking care of not staining the areas to be tested due to the heat generated during curing.

The human larynges were provided by the Anatomy Donation Program of the University of Hamburg-Eppendorf, Germany, in accordance with the Human Tissue Act [24]. The sample measurements at the Institute for Biomechanics of BGU Murnau were approved by the Ethics Committee of the State of Bavaria, Germany. The Declaration of Helsinki has always been respected [25].

The measurements ($n = 12$) of the human samples (age and sex unknown) were performed on a total of 18 human samples, excluding those of obviously damaged or deformed larynges (forensic medicine donations). Samples were stored at $-37\,^{\circ}$C, thawed 24 h before preparation, embedded in polyurethane (Rencast FC53 A/B, Huntsman Advanced Materials, Basel, Switzerland) immediately after preparation (by pouring the cricoid anterior arch) and measured to avoid tissue altering "freeze-thaw" cycles [26]. Care was taken not to alter the relevant tissue by the polyurethane resin.

***3) Force Measurement and Testing:*** Penetration of the cricoid cartilage occurred at the lamina, lateral to the central vertical ridge, in the middle of the depressions and in the direction from posterior to anterior (Fig. 2(a)). The angle of penetration was chosen perpendicular to the cartilage surface. This approach ensures no additional forces other than those in the insertion direction, also because the LPIT is stable enough not to deform. A K-wire with a diameter of 1.6 mm was chosen as penetration tool, as it corresponds to the geometry of the LPIT used for surgeries. The tool was attached directly to the load cell with a needle holder, co-centric to the load cell with identical force axes. The test speed was at 10 mm/min with a preload of 0.1 N, and the specimens were positioned in such a way that the entire cartilage was pierced when the measurement was completed. Thus the entire tip of the penetration tool was visible on the opposite side. During the measurements of one type of specimen, the penetration tool was not changed. The force curve was recorded as a function of the penetration depth into the cartilage. All measurements were performed according to this principle.

The measurement data of porcine larynges ($n = 12$, two measurements from each of six samples, one on each side of the almost symmetrical larynxes) as well as those of the artificial cricoids ($n = 6$, same fixation as the porcine samples) were generated with a uniaxial testing machine (Zwick Z005, Zwick/Roell GmbH & Co. KG, Ulm, Germany) with a force transducer (Zwick/Roell Xforce HP 200 N, Zwick/Roell GmbH & Co. KG, Ulm, Germany which meets the criteria of accuracy classes according to ISO 7500-1). The measurement of the human laryngeal samples was carried out in the same way as the porcine samples except that the testing machine was a Zwick Z010 (Zwick/Roell GmbH & Co. KG, Ulm, Germany).

In addition, experts (otorhinolaryngology surgeons collaborating with the MED-EL company) also assessed the haptics of the artificial cricoid cartilages.

### C. Smart Artificial Soft Tissue

The central element of the simulator is an artificial soft tissue layer, positioned behind the cricoid cartilage instead of the PCA muscle, determining LPIT's position within it.

***1) Hardware:*** The basic idea is to achieve electrical conductivity of an artificial soft tissue layer in order to use it as resistive sensor mat and detect voltage-carrying tools. Such a soft and elastic layer can be realized by incorporating conductive particles like carbon black into silicone [27]. In principle, various silicones corresponding to the mechanical requirements

of the tissue to be imitated can be used, but it should be noted that the modulus of elasticity of the composite also increases as the carbon black content increases [28]. The more carbon black is added to the silicone, the better the conductivity [29]. The base material used here is Ecoflex 35 fast (58 wt%, from Smooth-On, Inc., Macungie, PA, USA). In addition, isooctane (25 wt%, 2,2,4-Trimethylpentan ($\geq$ 99%) from Sigma-Aldrich, Inc., St. Louis, USA), Thinner (8.7 wt%) and Slo-Jo (0.8 wt%) (both from Smooth-On, Inc., Macungie, PA, USA) were added. Isooctane and Thinner reduce the viscosity of the liquid silicone, and Slo-Jo prolongs the polymerization time to ensure complete mixing before the silicone is cured. Carbon black (7.5 wt%, XPB 545 POWDER from ORION Engineered Carbons GmbH, Frankfurt, Germany), low dosed to hardly affect the haptics of the silicone, was used as conductive phase. Homogeneous mixing [30] was achieved using a speedmixer (DAC 600.2 VAC-P from Synergy Devices Limited, High Wycombe, United Kingdom) and low pressure (350 hPa). This resulted in a Specific Conductance of $\sigma = 10\,\mathrm{mS} \cdot \mathrm{m}^{-1}$ for conductive layers (sensor mats).

Various tasks can be covered by such sensor mats. In the simplest case, only a basic circuit is closed by a contact between a sensor mat and an insertion tool to detect when the tool reaches a certain position in the artificial tissue. By dividing the sensor mat into several areas, a first approach for localization, similar to Esterer et al. [31] can be realized. Therefore, only one electrode per sensor mat is sufficient.

In a next step, one-dimensional position detection can be obtained by using the conductive silicone composite as a rectangular layer with two elongated electrodes on opposite sides. Insertion tools can be used to apply voltage somewhere between the electrodes. This allows the measurement of currents that are inversely proportional to the ratio of the distances between the insertion point and the electrodes. Alternatively, by applying an electrical gradient field via the electrodes, a voltage, corresponding to the distances between the electrodes, can be tapped by insertion tools, similar to a potentiometer. This approach can also be extended to the two-dimensional case by using two orthogonal layers [32], [33].

To achieve a two-dimensional resolution, it is possible to use four punctual measuring electrodes ($P_i$, $i = 1..4$), inserted in the corners of a single, rectangular sensor mat as shown in Fig. 3. This method is used in the LP-simulator and is considered in more detail. In contrast to O'Neill et al. [34], no voltages are injected into the electrode pins when determining the position, but a constant voltage $U_N$ is injected into the sensor mat by a voltage-carrying injection tool (the LPIT) at point $P_N$. This variant closely represents real conditions, in which the muscles are stimulated by electrical currents from the LPIT. The distribution of partial currents on electrode pins are measured by voltages $U_i$ on shunt resistors $R_S$. Additionally, contact resistances $R_{Ci}$ between sensor mat and electrode pins as well as LPIT $R_{CN}$ must be taken into account. By these measurements, resistances $R_i$, which depend on the distances $r_i$ between LPIT tip and electrode pins can be utilized for position determination.

***2) Framework for Position Detection:*** Four resistance mappings $R_i(\vec{p}_N)$ are assumed for the resistances between LPIT tip and the electrode pins $P_i$ depending on LPIT tip position $\vec{p}_N = (x, y)$, with the coordinate origin in the sensor mat center (Fig. 3). These mappings can be obtained either from resistivity measurements, from finite element simulations, or from simplified model considerations. From them, the LPIT $x$-coordinate can be estimated by a general position reconstruction field

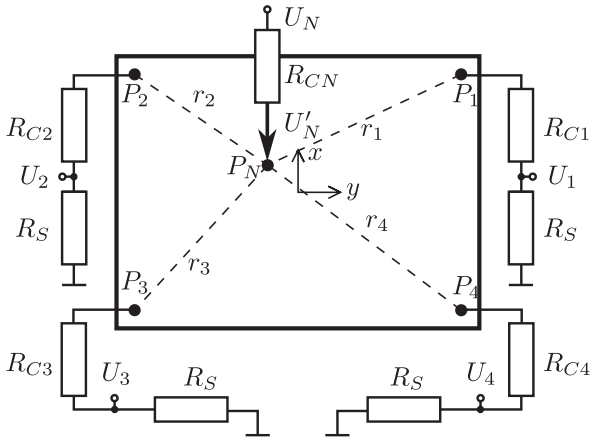


Fig. 3. Electrical circuit diagram of the sensor mat with electrode pins $P_i$, $i = 1 \ldots 4$ and LPIT insertion point $P_N$. Distances $r_i$ are defined by $\overline{P_N P_i}$ and measured pin voltages are given by $U_i$. Specific contact resistances for pins and LPIT are $R_{Ci}$ and $R_{CN}$ respectively. $R_S$ denotes a known shunt resistance.

$$\vec{f}(\vec{p}_N) = \vec{\phi}\,(R_1(\vec{p}_N), \ldots, R_4(\vec{p}_N)) \tag{1}$$

to be defined, which depends on all $R_i(\vec{p}_N)$, where its components must be strictly monotonic with respect to the $x$- and $y$-coordinate respectively. The LPIT tip position can then be reconstructed from $\vec{\phi}$ by inversion $\vec{p}_N = \vec{f}^{-1}(\vec{\phi}(R_1, \ldots, R_4))$ or better by approximation of the inverse mappings with suitable functions. The freedom to define function $\vec{\phi}$ in (1) can be used to achieve a position reconstruction mostly independent from unknown and typically varying contact resistances $R_{Ci}$ and $R_{CN}$ respectively. Finally the sensor resistances $R_i$ are not measured directly and thus they are estimated by pin voltage readings $U_i$. Contact resistances $R_{Ci}$ are obtained from a calibration routine (chapter II-C6), which has to be executed before using the sensor system.

***3) Finite Element Simulation:*** In order to gain the resistance mappings $R_i(\vec{p}_N)$ the smart artificial soft tissue was simulated with the Finite Element Method. A two-dimensional approach for the unwound mat was chosen since the thickness of the mat ($s = 1.5$ mm) is small compared to its outer dimensions. Moreover, the cylindrical, gold-plated electrodes with smooth surface completely penetrate the mat, which is why the geometry to be simulated is constant in the Z-direction. The simulation was carried out with Matlab's Partial Differential Equation Toolbox [35] with Gauss's law describing electrostatics of conductive materials

$$\sigma \nabla^2 V = 0 \text{ in } \Omega \tag{2}$$

with $\vec{n} \cdot \nabla V = 0$ on $\partial\Omega_B$, $\vec{n} \cdot (\sigma \nabla V) = -\sigma_i V$ on $\partial\Omega_E$ and $V = U'_N$ on $\partial\Omega_N$. Hereby $V(x, y)$ is the electric potential, $\sigma$

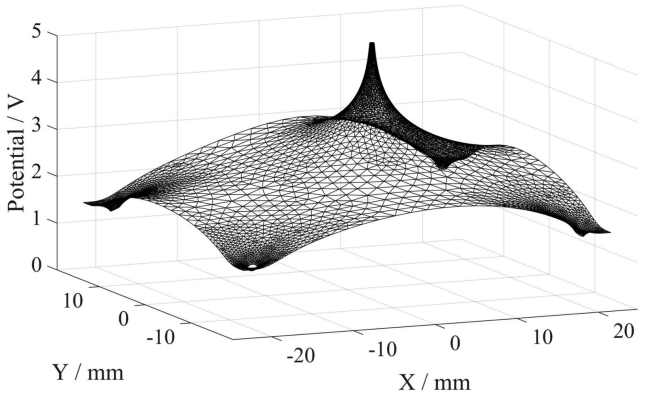


Fig. 4. Finite element simulation of the electrical potential field $V(x, y)$ in the sensor mat. The LPIT penetration point was at $x = 6$ mm and $y = 5$ mm. The dimensions of the sensor mat are $45$ mm $\times 35$ mm where the electrode pins are placed $2.5$ mm away from the outer edges of the mat in each direction achieving $L = 20$ mm and $W = 15$ mm respectively.

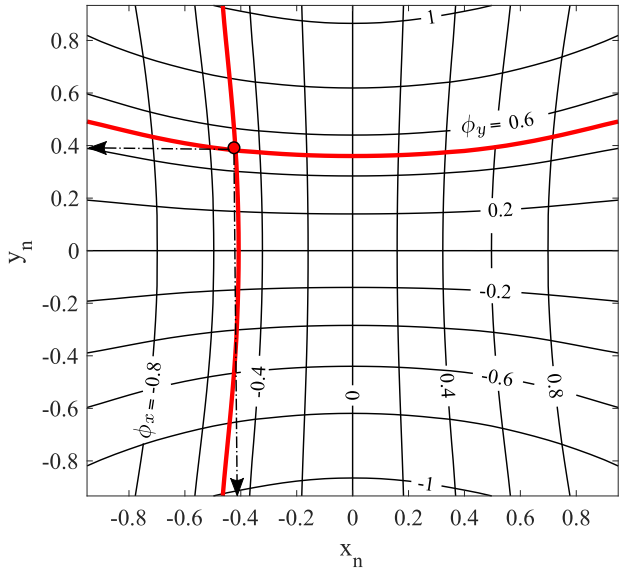


Fig. 5. Contour plot for position reconstruction field components $\phi_x$ and $\phi_y$ depending on normalized LPIT coordinates $x_n$ and $y_n$. The location of intersection of the contour lines $\vec{\phi} = (-0.5, 0.5)$ corresponds to the desired normalized LPIT coordinates $\vec{p}_N = (-0.4, 0.4)$.

the conductivity of the sensor mat and $\sigma_i$ the conductivity of electrode pin $P_i$. The pin diameter was chosen as $d = 1$ mm and the rectangular area spanned between the pins as $2\,L \times 2\,W$, $\Omega$ denotes the entire sensor domain and $\vec{n}$ is the normal vector to the boundary $\partial\Omega$. The free border of sensor mat $\partial\Omega_B$ as well as electrodes $\partial\Omega_E$ were Neumann boundary conditions, where the current density for shunt and contact resistance is defined by $\sigma_i V$. The pin conductivity $\sigma_i$ was obtained from series connection of $R_{Ci}$ and $R_S$. On LPIT contact point $\partial\Omega_N$ a Dirichlet boundary condition defined the injected LPIT voltage $U'_N$. Fig. 4 shows the field $V(x, y)$ for a rectangular sensor domain. Due to shunt resistors $R_S$, the potential is drawn towards ground at the four electrode pins located at sensor mat corners, while the voltage-carrying LPIT pulls the electrical potential towards supply voltage.

***4) Position Reconstruction Field:*** A possible choice for the reconstruction field $\vec{\phi}$ relies on the simplified model assumption that the electrical resistances $R_i$ between LPIT tip $P_N$ and electrode pin locations $(P_i,\ i = 1\ldots4)$ as illustrated by Fig. 3 are proportional to the corresponding distances $r_i = \overline{P_N P_i}$. By simple geometrical considerations the normalized coordinates $x_n = x/L$ and $y_n = y/W$ can be obtained from distances $r_i$ as follows

$$x_n = \frac{r_1^2 - r_2^2}{(2L)^2} = \frac{r_4^2 - r_3^2}{(2L)^2}, \tag{3}$$

$$y_n = \frac{r_3^2 - r_2^2}{(2W)^2} = \frac{r_4^2 - r_1^2}{(2W)^2}, \tag{4}$$

where $2L$ and $2W$ are the distances between the electrodes respectively. Since $R_i = \rho/A\ r_i$, where $\rho$ denotes the specific electrical resistance and $A$ a cross-sectional area assumed to be constant, distances in (3)–(4) can be approximated by corresponding resistances. In order to achieve a reconstruction field which is mainly independent on contact resistances the following strictly monotonic field $\vec{\phi} = (\phi_x, \phi_y)$ is proposed

$$\phi_x = \frac{1}{2}\left(\frac{\Delta\alpha_1^2 - \Delta\alpha_2^2}{\Delta\alpha_{hor}^2} + \frac{\Delta\alpha_4^2 - \Delta\alpha_3^2}{\Delta\alpha_{hor}^2}\right), \tag{5}$$

$$\phi_y = \frac{1}{2}\left(\frac{\Delta\alpha_3^2 - \Delta\alpha_2^2}{\Delta\alpha_{ver}^2} + \frac{\Delta\alpha_4^2 - \Delta\alpha_1^2}{\Delta\alpha_{ver}^2}\right). \tag{6}$$

Here $\Delta\alpha_i = \alpha_i - \alpha_{i,min}$ denotes the range of the position dependent resistance ratio $\alpha_i$ for pin $P_i$ with

$$\alpha_i = \frac{\hat{R}_i}{\sum_{i=1}^{4}\hat{R}_i},\ \hat{R}_i = R_i(\vec{p}_N) + R_{Ci} + R_S. \tag{7}$$

The value $\alpha_{i,min}$ is the resistance ratio $\alpha_i$ if the LPIT is placed next to pin $P_i$, where the position dependent resistance $R_i$ will tend to zero. The mean horizontal range $\Delta\alpha_{hor} = \text{mean}(\Delta\alpha_{1,hor}, \Delta\alpha_{4,hor})$ considers with $\Delta\alpha_{i,hor} = \alpha_{i,max} - \alpha_{i,min}$ the horizontal distances of the electrodes. Here, $\alpha_{i,max}$ is obtained when the LPIT is placed next to the horizontally adjacent pin of $P_i$ such that the position-dependent resistance $R_i$ is maximized (for purely horizontal deflection). Consequently $\Delta\alpha_{ver} = \text{mean}(\Delta\alpha_{3,ver}, \Delta\alpha_{4,ver})$ defines resistance ratio ranges between vertical adjacent pins. All these values can be obtained during a calibration procedure prior to the usage of the sensor system as discussed in the sequel.

Fig. 5 shows the contour plot of $\phi_x$ and $\phi_y$ respectively obtained from simulation of the sensor mat with conductivity ratio $\gamma = \sigma_i/\sigma = 1.0$. Since $\phi_x$ and $\phi_y$ obtained from (5)–(6) are closely related to normalized coordinates $x_n$ and $y_n$, the reconstruction field components can be utilized to reconstruct the LPIT position. Observing the contour lines for $\vec{\phi} = (-0.5, 0.5)$ highlighted in Fig. 5, it can be perceived that the $x-$ and $y-$coordinates of their intersection $(-0.4, 0.4)$ are the desired LPIT coordinates. If the grid defined by the contour lines of reconstruction field defined a regular, orthogonal grid, the normalized LPIT coordinates would be directly taken from the field components $\phi_x$ and $\phi_y$ respectively. However, due to boundary effects this is only true in a small region around the center of

the sensor mat. Near to the edges of the sensor the contour lines are distorted. Therefore for position reconstruction the inverse of $\vec{f}$ provides the desired instrument coordinates. Since the resistance mappings for the reconstruction field are available, its inversion can be approximated by suitable functions to obtain the instrument coordinates as

$$x_n = f_x^{-1}(\phi_x, y_n) = \left(a_x + b_x \phi_x^2 \exp(c_x y_n^2)\right) \phi_x \quad (8)$$

$$y_n = f_y^{-1}(x_n, \phi_y) = \left(a_y + b_y \phi_y^2 \exp(c_y x_n^2)\right) \phi_y \quad (9)$$

with parameters $\vec{\theta} = (a_x, \ldots, c_y)$ to be determined by fitting these functions to data obtained from simulation. To account for different sensor mat conductances $\sigma$ and pin conductances $\sigma_i$ numerous simulations for different ratios $\gamma = \sigma_i/\sigma$ in the interval $\gamma \in [0.1, 2.5]$ were performed. In case of a quadratic sensor domain with $L = W$ the parameters were equal for both reconstruction fields due to symmetry reasons, therefore $a_x = a_y$, $b_x = b_y$ and $c_x = c_y$. For reasons of clarity, the parameter estimation was performed for such quadratic sensor domains with different values for $L$ in the interval $L \in [30, 100]$ mm with step size of 5 mm.

For each simulation setup and therefore conductivity ratio $\gamma$ and $L$ the unknown parameter vector $\vec{\theta}(\gamma, L)$ was determined by a nonlinear least squares method (Levenberg-Marquardt Algorithm, [35]). The model quality for all performed parameter estimations was quantified by $q = 1 - min(\|\hat{y} - y\|/\|y\|, 1)$ where $y$ denotes used reference values and $\hat{y}$ the fitted ones. Assuming a given conductivity ratio $\gamma$, then the latter defined inverse functions were derived by obtaining the parameter vector $\vec{\theta}(\gamma, L)$ from computed parameter vectors by linear interpolation. Thus the position detection method is able to adopt to a current system setup, where the sensor mat conductivity, as well as pin contact resistances may have been changed since last the application. In turn the instrument position can be obtained by solving equation system (8)–(9) for $x_n$ and $y_n$ respectively, which is practically obtained by computing the intersection of both equations.

***5) Voltage Readings:*** Pin voltages $U_i$ are measured by means of four shunt resistors $R_S$ with a 10 b analogue digital converter of the microcontroller (ATMEGA 32U4, Atmel Corporation, San Jose, USA). From the electrical circuit diagram in Fig. 3 one can conclude that $\hat{R}_i = U'_N/U_i \cdot R_S$. Therefore the ratio $\alpha_i$ as defined by (7) can be obtained directly from voltage readings as

$$\alpha_i = \frac{U_i^{-1}}{\sum_{i=1}^{4} U_i^{-1}}, \quad (10)$$

which becomes completely independent from $U'_N$ and thus from LPIT contact resistance $R_{CN}$. From a practical perspective this is critical for success, since the LPIT contact resistance depends on the intensity of LPIT contact or penetration as well as on non-conductive particles which may influence the conductivity between LPIT tip and sensor mat. These influences would have a strong impact on the accuracy of the position reconstruction.

***6) Calibration:*** Before a simulated surgical procedure using the Smart Artificial Soft Tissue for LPIT position tracking can be started, a newly inserted sensor mat has to be calibrated to compensate for any deviations of the sensor mat's conductivity or changed contact resistances. Since the contact resistance between the electrodes and the carbon black-silicone composite depends mainly on the geometry and material of the elements and particles in contact [36], a constant and equal contact resistance $R_{Ci} = R_C$ for $i = 1 \ldots 4$ is assumed. The fact that the sensor mat is fixed in the area of the electrode pins by a fastening clamp and thus very limited deformations or movements are possible in these areas supports this assumption. Further it is assumed that the conductivity $\sigma$ of the sensor mat remains constant over a normal period of usage.

For calibration the LPIT is placed onto the sensor mat as closely as possible to each of the four electrode pins $P_i$ which provides ratios $\alpha_{i,min}$ and $\alpha_{i,max}$ as required by equations (5)–(6) where ratio $\alpha_i$ is obtained from voltage readings according to (10). Hereby several voltage readings are averaged over a certain time period in order to obtain more robust results. All other ratios for $\Delta\alpha_{hor}$ and $\Delta\alpha_{ver}$ can be obtained accordingly.

In addition, it is important that all contact resistances $R_{Ci}$ are equal and sufficiently small. This can be checked by the microcontroller's general purpose I/O pins. If the LPIT is placed next to a pin it is set to the supply voltage $U_0$ while all others pins are set to ground. Switching the I/O pin connected to the LPIT to high impedance input allows to measure the mat voltage $U_{Ni}$ by the LPIT tip. Denoting the mat resistance between active pin $P_i$ and all other pins with $R_{||}$, which is serial to the contact resistance $R_{Ci}$, results in

$$\frac{R_{Ci}}{R_{mat}} \approx \frac{1}{3}\left(\frac{U_0}{U_{Ni}} - 1\right). \quad (11)$$

This assumes that $R_{||} \approx 1/3\, R_{mat}$ and thus the resistance to all adjacent pins is approximately equal. This ratio can be utilized to estimate the size of the contact resistance. If the ratio in (11) is below 0.1, the contact of the sensor mat is considered to be sufficient.

Another characteristic parameter of the sensor mat to be determined is the conductivity ratio $\gamma$, which is the ratio of pin conductivity $\sigma_i$ to mat conductivity $\sigma$. The pin conductivity is related to the series connection of contact and shunt resistance. Simulation experiments revealed that this ratio can be estimated from

$$\gamma = k\left(\frac{1}{U_i/U_j - u_0} - 1\right) \quad (12)$$

where $U_j$ denotes the voltage at pin $P_j$ $(j = 1 \ldots 4)$, where the voltage driven LPIT is placed in its immediate proximity and $U_i$ denotes the voltage measured at the diagonal adjacent pin $P_i$. Hereby the parameters $k$ and $u_0$ can be obtained by nonlinear least squares estimation from simulation experiments for different $\gamma$. Since the required voltage readings in (12) can be obtained during the calibration procedure, the conductivity ratio is defined for the sensor mat in use. Consequently the parameters for inverse functions (8)–(9) can be obtained from linear interpolation which in turn allow to compute the LPIT position by the proposed framework.

***7) Verification and Validation:*** The proposed position reconstruction method was verified by simulation experiments.

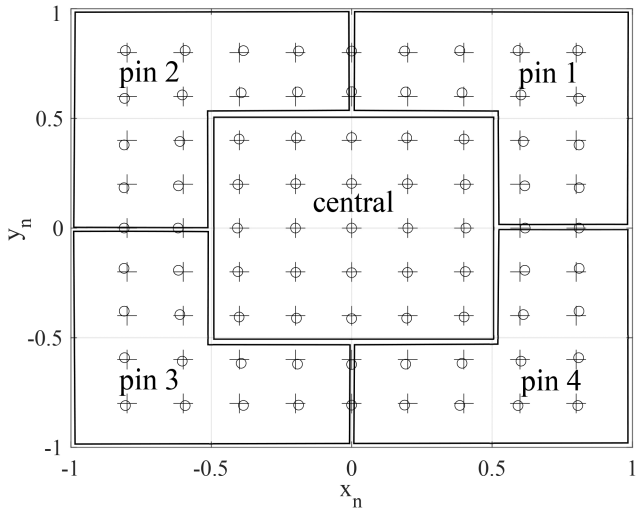


Fig. 6. Comparison of predefined and reconstructed LPIT positions: (+) denotes the exact and (o) the reconstructed position. The sensor mat is divided into a central and four pin regions in order to compute the region specific accuracy.

TABLE I
SIMULATED POSITION RECONSTRUCTION ACCURACY: MEAN ERROR AND STANDARD DEVIATION IN % OF NORMALIZED COORDINATES FOR CENTRAL AND PIN REGIONS

| case | central | pin 1 | pin 2 | pin 3 | pin 4 |
|---|---|---|---|---|---|
| I | 0.23±0.14 | 0.72±0.10 | 0.72±0.10 | 0.72±0.10 | 0.72±0.10 |
| II | 0.29±0.20 | 0.76±0.26 | 0.76±0.26 | 0.76±0.26 | 0.76±0.26 |
| III | 2.20±1.31 | 1.25±0.35 | 3.00±1.41 | 6.46±1.51 | 3.61±1.28 |
| IV | 1.88±1.11 | 1.13±0.60 | 2.57±1.12 | 4.74±0.96 | 2.77±1.31 |
| V | 3.79±1.89 | 1.89±1.05 | 4.43±2.10 | 9.98±2.27 | 7.65±2.33 |

The accuracy of the position reconstruction was quantified by the mean error with respect to desired, normalized positions. In order to investigate the results from different parameter studies the sensor mat was divided into five regions, one central region and four electrode pin regions as indicated in Fig. 6. Especially the central region was important for the application in mind, since the PCA muscle resides in this region and thus an accurate LPIT position was important for hotspot detection. Within these regions the average of the mean error and its standard deviation were computed. Hence, it was possible to investigate the influence of different parameter settings on the accuracy of the reconstruction method. Five different cases were examined for this purpose, which will be discussed in more detail in the description of Table I (chapter III-B1).

For validation purposes the proposed position detection method was implemented on ATMEGA 32U4 in C++. A template with $7 \times 9$ equidistant positions in a range of 32 mm $\times$26 mm around the origin was printed and placed over the sensor mat inside the opened simulator case. Then the LPIT was placed on the predefined positions where the computed LPIT position in turn was transmitted over the serial interface to the simulator software and stored for further processing. These measurements were repeated on twelve identically manufactured sensor mats. The mean error and the corresponding standard deviation were computed for the referenced regions.

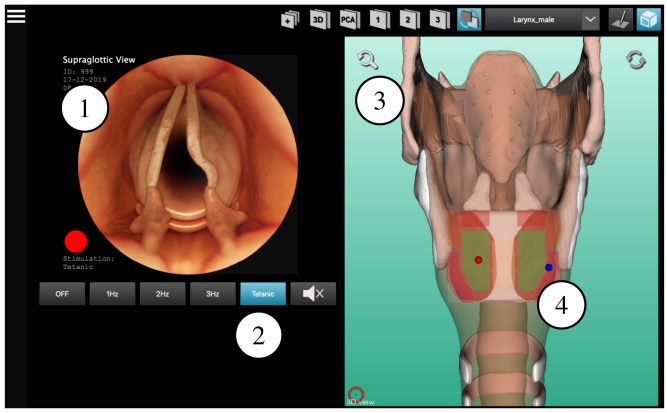


Fig. 7. Software as virtual part of the simulator. (1) Vocal fold animation, (2) Stimulation control buttons, (3) 3D-view of the anatomy, (4) Display of insertion points (blue and red dot).

## D. Virtual Simulator Components

The software for the hybrid simulator as shown in Fig. 7 is based on Qt-C++ Framework (Version 5.12.4) using VTK (Version 8.2.0) for 3D-visualization. The user interface is divided into different areas. On the left, during the initial part of the insertion phase, a live video stream of an endoscope is shown in order to monitor the tunneling of the LPIT under the synthetic mucosa of the laryngeal phantom. When penetrating the cricoid surface, one can proceed to a virtual simulation of the endoscopically observed vocal folds (1). Depending on the position of the LPIT, different movement patterns of the vocal folds are induced by electrical stimulation. When the hotspot is reached by the LPIT, the vocal folds move laterally and thus simulate an opening of the glottis. Otherwise the simulation shows an adverse reaction e.g. closing of the vocal fold or a mixed reaction of closing and opening. Buttons for controlling the electrical stimulation (OFF/1 Hz/2 Hz/3 Hz/Tetanic) are positioned underneath (2). Optionally an acoustic signal indicating the stimulation impulses can be enabled. Both, endoscope view and control elements for electrical stimulation are typically available for the real surgical intervention. The right side of the user interface provides additional information to support teaching and learning. The 3D anatomy view of the larynx (3) can be rotated, moved and zoomed by the trainee which supports learning anatomy or helps to identify critical anatomic regions. The core task, the correct positioning of the LPIT into the PCA muscle, can be facilitated by the view of target areas (4). The positions of the LPIT tip in the PCA muscle are indicated by red and blue dots, since two electrodes are supported and thus the correct positioning of the instrument tips can be verified easily. The target areas or hotspots are colored green while sub-optimal areas are colored orange or red.

## E. Physical Simulator Components

A phantom combining hybrid requirements as well as haptics and position recognition with their components is shown in Fig. 8 (Housing and support structures made of 3D-printed Ultimaker Tough PLA from Ultimaker B.V., Utrecht, Netherlands). The

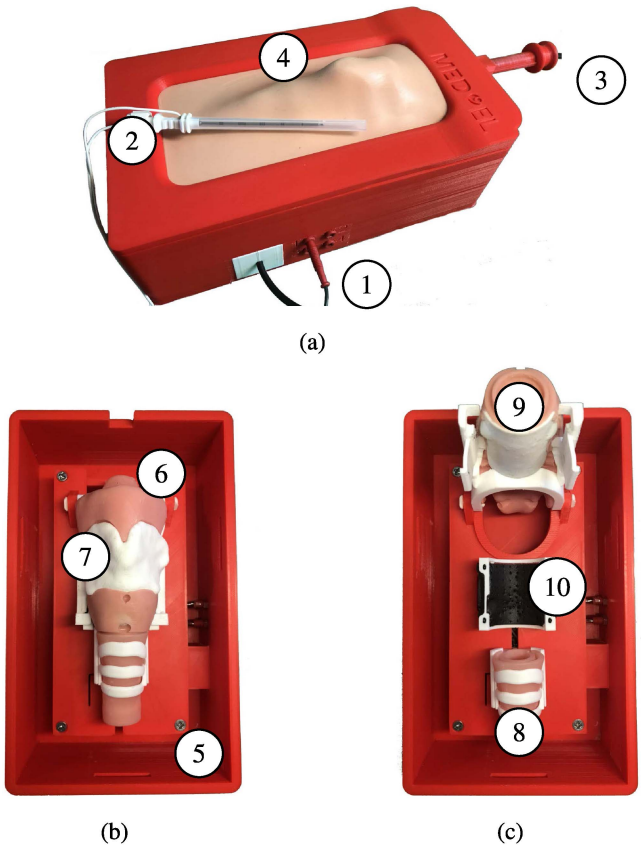


Fig. 8. Inner structure of the physical simulator part, housing dimensions ($L \times B \times H$): $L = 200$ mm, $B = 120$ mm, $H = 70$ mm; (a) closed and ready to use system, (b) opened simulator, (c) disassembled inner anatomies. (1) connections for LPITs and USB-interface, (2) LPIT, (3) USB-endoscope, (4) artificial skin, (5) base plate with integrated circuits, (6) simplified representation of thyroid membrane, hyoid bone and epiglottis, (7) thyroid cartilage, (8) ligamentum cricotracheale with cartilage rings, (9) artificial, replaceable cricoid cartilage, (10) sensor mat.

physical simulator can be connected to the other simulator components via the laterally mounted connectors (1). A micro USB port connects the micro controller to the computer and the simulator software. The LPITs (2) are connected via 1.5 mm banana plugs (1). Four connectors allow to connect two LPITs consisting of canula (outer part) and trocar (inner part) each. The canula shows a backward offset of 3 mm and is electrically insulated from the trocar. Thus the canula can be used to detect whether the LPIT was inserted too deeply representing a penetration of the esophagus. A USB-endoscope (3) provides a sub- and supra-glottic view into the simulator's interior. By removing the artificial skin (4), the inner structures of the simulator become visible. The base (5) contains the electronic circuits and the micro controller. The elements (6), (7) and (8) are not penetrated during simulation. Thus they are made of more durable material. In contrast, the cricoid with its adjacent tissue (9), which has to be changed regularly, as well as the sensor mat underneath (10) require a realistic haptic perception when inserting the LPIT into the artificial anatomy. These wear parts can be replaced by lifting the parts (6) and (7) upwards and sliding the artificial trachea

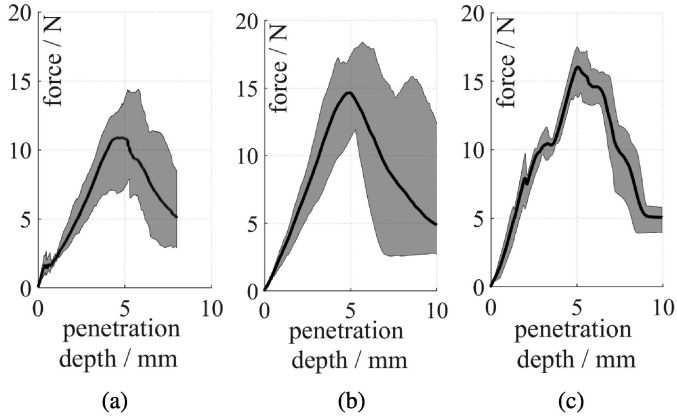


Fig. 9. Force measurements during penetration of the cricoid cartilage with a needle geometrically corresponding to the LPIT. The arithmetic mean (black line within the gray area), minima (lower boundary of the gray area) and maxima (upper boundary of the gray area) are shown. (a) Measurements from human samples, (b) measurements from porcine samples (c) measurements from artificial cricoid.

(8) downwards. After reassembly, the structures are covered with synthetic skin (4) and soft tissue again.

## III. Results

### A. Tissue Measurements

The artificial cricoids and the human and porcine specimens were compared on the basis of four characteristics: Maximum force, number of dominant peaks, peak distance and the morphology of the measurement curve (Fig. 9). For haptic evaluation, in both the human (Fig. 9(a)) and the porcine samples (Fig. 9(b)), one dominant peak between 10 N and 15 N was detected. Thereby the forces in the porcine samples (maximum of mean force curve $\tilde{f}_{max} = 14.7$ N; [range $12.0-18.4$ N]) were slightly higher than in the human samples ($\tilde{f}_{max} = 10.9$ N; [range $7.9-14.4$ N]), although the force ranges of the individual measurements partially overlapped. In addition, a characteristic, small and sharp peak at the beginning of the measurement curve ($< 1$ mm) was noticed in the human samples. From the distance between the two peaks or from onset to the dominant peak, the sample thickness of about 5 mm can be estimated.

With the help of surgical experts, different material compositions were evaluated and the artificial cricoid introduced in chapter II-B1 was identified as the most realistic imitation (Fig. 9(c)). As with the human samples, the artificial cricoid (Fig. 9(c)) proved the second peak ($\tilde{f}_{max} = 16.02$ N; [range $14.1-17.4$ N]) to be more dominant than the first. Furthermore, spacing between the two peaks was similar to the human samples. Although similarly sharply edged, the first peak of the artificial was somewhat higher than the human one. The maximum force corresponds to those of the biological references.

### B. Smart Artificial Tissue

***1) Simulation:*** The parameters for the inverse functions according to (8)–(9) were computed for 16 different dimensions of the sensor mat with 16 different conductivity ratios $\gamma$ for

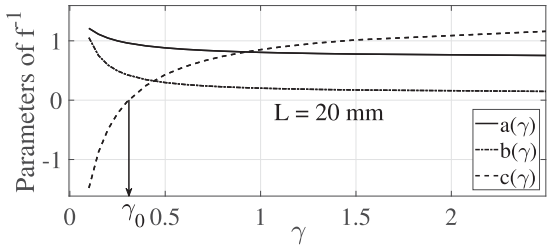


Fig. 10. Parameters for approximation of $f_x^{-1}$ and $f_y^{-1}$ for a quadratic sensor domain as a function of conductance ratio $\gamma$. The different conductance ratios were obtained by changing conductances of pin contact resistance and sensor mat accordingly.

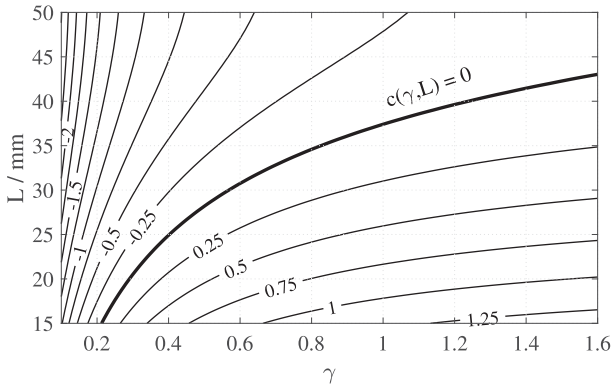


Fig. 11. Contour plot of parameter field $c(\gamma, L)$. The conductivity ratio where the parameter field $c$ is zero is denoted as $\gamma_0(L)$. For this configuration the distortion of the reconstruction grid is minimized.

each simulation case. The mean value of the model quality $q$ for all 256 models obtained from nonlinear optimization was $97.04 \pm 0.46\%$ for $f_x^{-1}$ and $f_y^{-1}$ respectively.

Generally, the parameters $a, b$ and $c$ for a quadratic sensor domain with $L = 20\,mm$ depending on the conductivity ratio $\gamma$ are depicted in Fig. 10. The parameter $c$ is directly related to the distortion of the grid given by the contour lines of the reconstruction field $\vec{\phi}$ as depicted in Fig. 5. For $c < 0$ a concave grid distortion results from rather high pin contact resistances and for $c > 0$ a convex distortion is obtained for lower contact resistances. If parameter $c = 0$, then the distortion of the reconstruction grid is minimized. Fig. 11 depicts the contour lines for the parameter field $c(\gamma, L)$. The contour line where $c = 0$ denoted by $\gamma_0(L)$ represents an adjusted sensor system, where the distortion of the reconstruction grid is minimized. The adjustment can be done by changing the shunt resistances so that the conductivity ratio $\gamma = \gamma_0(L)$. Parameter $a$ is connected to the slope of the reconstruction field around the origin and parameter $b$ represents boundary effects along the edges of the sensor domain. Both parameters and the diagonal voltage ratio $U_i/U_j$ are shown in Fig. 12(a) for an adjusted sensor system along $\gamma_0$ for different sensor domain dimensions $L$. The diagonal voltage ratio according to (12) represents the ratio between smallest and highest possible pin voltages. The smaller this ratio, the higher the sensitivity of the position reconstruction method.

The conductivity ratio $\gamma$, which turned out to be a characteristic parameter, can be estimated by (12) for different sizes

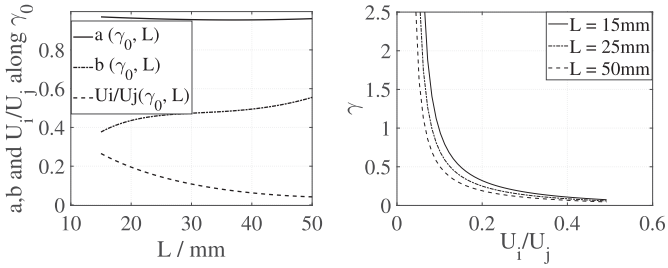


Fig. 12. Parameters and their dependencies (a) Parameters $a(\gamma_0, L)$, $b(\gamma_0, L)$ and diagonal voltage ratio $U_i/U_j(\gamma_0, L)$ for an adjusted sensor system, (b) Conductivity ratio $\gamma$ depending on voltage ratio $U_i/U_j$ during calibration for different sensor domain dimensions $L$.

$L$ of the sensor domain by means of calibration readings. The mathematical model was fitted to simulation data. The result is depicted in Fig. 12(b) and shows the conductivity ratio depending on diagonal voltage ratio for different dimensions $L$. Hereby a model quality of $99.74\%$ was achieved. Concluding, the proposed position reconstruction algorithm is summarized by the following steps: i) First perform the calibration routine and obtain the conductivity ratio $\gamma$ according to Fig. 12(b), then ii) from parameter fields $a(\gamma, L), b(\gamma, L)$ and $c(\gamma, L)$ as depicted in Fig. 11 and 10 get the reconstruction field parameters, and iii) compute function (8)–(9) from voltage readings according to (10) and obtain the normalized instrument coordinates $x_n$ and $y_n$ respectively.

This algorithm was performed for different simulation cases, where the mean and standard deviation of the position reconstruction error in different regions of the sensor domain is summarized in Table I. The dimension $L$ of the quadratic sensor domain was $L = 20$ mm. Thus a $10\%$ error in normalized coordinates was an absolute error of $0.1\,L = 2$ mm. For case I, III-V the conductivity ratio was $\gamma = 0.15$, for case II $\gamma = 0.3$. Case I and II used a nominal contact resistance equal for all pins. Case III had $10\%$ contact resistance increase at pin $P_4$, case IV a $10\%$ decrease at pin $P_1$ and case V a $10\%$ decrease at pin $P_2$ in combination with a $10\%$ increase at pin $P_4$. For simulation cases I and II, where the pin contact resistance was equal for all pins, the accuracy in the central region was below $0.3 \pm 0.2\%$ in $\%$ of normalized coordinates. The error in the pin regions was approximately 2.5-fold higher as in the central region. Simulation cases III–V showed the effect of different pin contact resistances. The largest error was observed for case V in region pin 3 with $9.98 \pm 2.27\%$ in normalized coordinates. Hereby the pin contact resistance was reduced by $10\%$ at pin $P_2$ and at the diagonal adjacent pin $P_4$ the contact resistance was increased by $10\%$.

***2) Validation:*** To validate the position reconstruction using measurement data, twelve sensor mats were analyzed using a grid with $7 \times 9$ holes for predefined LPIT positions (Fig. 13). Based on these measurements, the mean errors and corresponding standard deviations in $\%$ of normalized coordinates (or in absolute values) were $7.04 \pm 3.28\%$ ($1.23 \pm 0.59$ mm) for the central region, $9.52 \pm 5.33\%$ ($1.59 \pm 0.85$ mm) for pin 1 region,

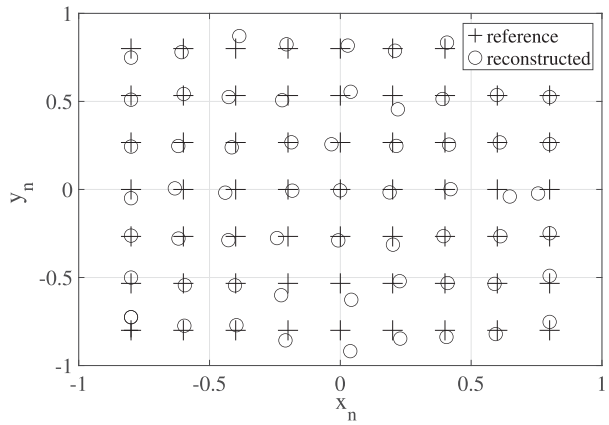


Fig. 13. Comparison between real position values (+) and measured positions (o) as average of 12 measurements. A grid of 7 x 9 with a grid size of 4mm in each direction was used.

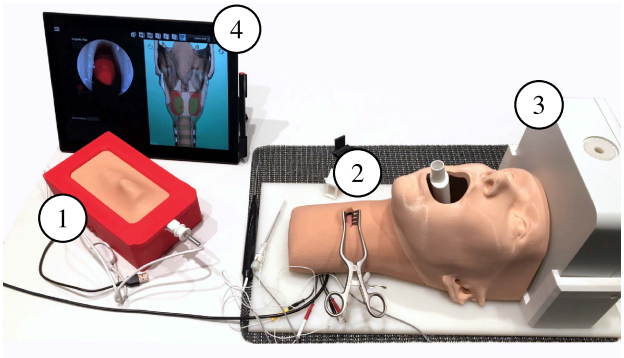


Fig. 14. Final simulator with all components; (1) simulator in box, (2) simulator with head and neck replica for more realism (high fidelity trainer), (3) electromagnetic position tracking system, (4) tablet-computer for virtual extension.

$9.44 \pm 6.02\%$ ($1.57 \pm 0.94$ mm) for pin 2 region, $9.18 \pm 5.18\%$ ($1.51 \pm 0.82$ mm) for pin 3 region and $9.57 \pm 5.11\%$ ($1.61 \pm 0.82$ mm) for pin 4 region respectively.

### C. Final Setup

The complete setup with two different versions of the simulator can be seen in Fig. 14. Either the simplified, more mobile version can be used (1), or the more advanced version (2), which is additionally equipped with electromagnetic tracking (3) (NDI Aurora, Planar 20-20 V2 from NDI Europe GmbH, Radolfzell, Germany) of the LPITs. The movements of the LPIT induced by the trainees can be tracked throughout the simulation and subsequently evaluated. This is achieved via sensor coils attached directly to the LPIT or other tools. The simulator's internal hardware, which enables realistic haptics as well as position detection of the insertion LPITs in the sensor mat, is identical for both variants. In the advanced variant, however, the use of a medical endoscope is possible, which can be inserted into the patient phantom via the replica of a laryngeal mask. In the simpler variant, the endoscope is replaced by a movable, inexpensive USB-endoscope. The software adapts to the variant used and can be integrated via an ordinary computer (4). To achieve the hybrid character of the simulator, the visual simulation of the vocal fold movement on the screen adapts to the position of the LPIT. Consequently, this connects the virtual and physical component, which, in turn, enables feedback on the surgery performed on the physical part. As shown in Fig. 14 (below (2)), additional surgical instruments such as spreader, forceps and needle holders can be used without limitation. Also sutures can be placed to mimic and train the implantation procedure more accurately.

## IV. Discussion

### A. Usability and Haptics

The main objective was to develop synthetic tissue with position evaluation capabilities (Smart Artificial Soft Tissue) with an associated easy-to-use surgical simulator for demonstration. The physical patient phantom with its realistic haptic perception during LPIT insertion must fulfill three prerequisites that are challenging to combine. First, all relevant anatomical parts should be manufactured as realistic as possible. Second, manufacturing effort should be kept as low as possible to be cost-effective. Third, the phantom must be easy to disassemble so that the wear parts, sensor mat and cricoid, can be easily replaced and the simulator can be simply reassembled afterwards (time consumption is less than two minutes). This ensures the reusability of most of the simulator, which is unfortunately not achieved by many other physical simulators [8]. These, as well as other previously mentioned requirements of the involved surgical experts and their feedback were integrated throughout this work. The needle insertion forces were mainly influenced by their experience [37] and verified by biomechanical measurements, also because no references from clinical practice are yet available due to the novelty of the intervention. Application examples of the simulator including videos can be found in the supplementary material. Regarding the reusability of penetrated parts such as the cricoid, it is known from Esterer et al. [31] that a significant drop in insertion forces occurs after 10-15 penetrations at identical insertion points. This behavior was also observed with the artificial cricoid. Since subsequent trainings on the simulator hardly lead to identical penetration points, it is proposed to change the cricoid and sensor mat after every 20-30 simulations.

The software is simple, symbolic, and can be operated entirely via touch screens. Like in real surgery procedures, various surgical instruments can be used additionally. This ensures maximum realism in terms of dexterity and haptics.

According to the experts, both peaks in the force progression of the artificial cricoid are essential, as two pressure points are always clearly notable when penetrating the cricoid. An optimisation of the force profile was achieved by the reduction of the wall thickness and the additional coating mentioned in chapter II-B1. This led to the crucial first peak. Thus, both the expert knowledge and the information of the measurement data were incorporated. As some natural spread is always present in organic tissues, the artificial cricoids are considered haptically similar enough (especially with regard to the characteristics mentioned in chapter III-A) to ensure realistic training.

The success of a surgery completed on the simulator can be read directly from the position of the inserted electrodes. The quality of the surgery can be quantified by the number of retractions or too deep penetrations.With the high-fidelity version, it is also possible to record the tool path directly inside the phantom for detailed analysis and discussion in a debriefing session.

### B. Calibration and Contacting Problems

The calibration of the sensor should compensate for inhomogeneities and take the changes of the contact resistances into account after replacing the sensor mat. High resistance contacts are caused, for example, by the concentration, distribution and shape of the conductive carbon black particles embedded in the silicone as well as the geometry of the contact point [36]. In contrast to others [34], the contact resistance between sensor mat and the electrodes was reduced by increasing the contact pressure of the clamp holding the sensor mat and by using gold electrodes. Increasing the diameter of the electrodes and thus the contact area also had a positive effect on the undesired resistances. Calibration requires to open and disassemble the simulator and to place the LPIT beneath the electrode pins. Calibration without manual intervention of the user could be realized with four double electrodes, which allows to measure the contact resistance directly. However, this would lead to considerably higher cabling and electronic hardware costs, especially if more than one sensor mat will be operated simultaneously.

### C. Positioning Accuracy and Further Application

In contrast to other, contact-based position sensing in hybrid simulators [31], the developed Smart Artificial Soft Tissue offers the advantages of continuous, two-dimensional position detection. The accuracy of the proposed position reconstruction method depends strongly on the conductivity ratio between electrode pins and sensor mat. Therefore it is recommended to adjust the shunt resistors accordingly to achieve a mostly undistorted reconstruction grid. The estimation of the conductivity ratio by means of calibration measurements allows to optimally adjust the reconstruction method to current operation conditions. The calibration routine should be performed once a day, typically when starting the simulator. Thus the usability is only slightly affected by performing the calibration procedure. The reconstruction accuracy is sufficient with an average deviation of 1.23 mm in the central region for accurate hotspot detection. Larger errors only occur along the borders of the sensor domain due to unavoidable local stresses on the sensor mat or inhomogeneities due to manufacturing inaccuracies. However, errors in these areas are not critical and hardly pose any problems for the simulated intervention. Since the optimal areas in the PCA muscles vary for different patients and have a size of about 9 $\times$ 18 mm, the accuracy is sufficient for an efficient training. Additional averaging of several measurements further increases the accuracy.

Bending of the carbon black-silicone composite hardly affects the results due to the thinness of the sensor mat in relation to the bending radius and the method of position determination. The resistance changes due to low strain and compression resulting from bending partially compensate, although not completely due to nonlinearity [28], [29]. The remaining minimal change in resistance is uniformly distributed over the mat and is compensated by the calibration (fitting the system to the general resistance conditions). These assumptions are confirmed by the results, since the morphology of the determined positions corresponds to that of the real positions.

With the actual setup, the pin voltages are measured directly with a 10-bit ADC of the used microcontroller, which limits the position accuracy, especially when small position changes occur or the LPIT is near the boundary of the sensor domain. The absence of more complex electrical circuitry is intended to demonstrate the robustness of this technology even under unfavorable conditions. To establish it as a basic element for future hybrid surgery simulators, the functionality was demonstrated with the simplest possible elements. A possible improvement would be the usage of differential amplifiers with programmable gains. This would allow to adopt the gains to maximize measurement resolution. A further accuracy improvement would be possible by introducing additional measuring electrodes along the boundary of the sensor mat. However, this would be accompanied by a higher system complexity and an increased number of components.

For future projects, the Smart Artificial Soft Tissue developed here can be used for various biopsy simulators or similar, in which conductive tools are inserted into tissue. This would provide a new basic element to accelerate the development of future hybrid surgical simulators as well as a post-simulation automatic evaluation capability that is missing in many physical simulators [8].

## V. Conclusion

Smart Artificial Soft Tissue offers a fundamental key element for hybrid simulators which was demonstrated by a surgical simulator for implanting the electrodes of a laryngeal pacemaker. The sensor technology is based on the inversion of resistance mapping between a conductive sensor layer made of carbon-black-silicone composite and a voltage carrying surgical instrument in contact. With this type of sensor technology, it is possible to extract relative position data from surgical instruments in haptically adapted soft tissue-mimicking artificial anatomies with sufficient accuracy.

## Acknowledgment

This work has been made possible by the support of Johannes Kagerer and Natalie Ing from MED-EL. Furthermore, the authoeers would like to thank Martin Winkler for his support in the preparation of the human specimens, Markus Samrykit for his support in the measurement of porcine specimens and Stefan Gabauer for his support with the initial prototype.

## References

[1] A. J. Lungu et al., "A review on the applications of virtual reality, augmented reality and mixed reality in surgical simulation: An extension to different kinds of surgery," *Expert Rev. Med. Devices*, vol. 18, no. 1, pp. 47–62, 2021.

[2] S. R. Dawe et al., "Systematic review of skills transfer after surgical simulation-based training," *J. Brit. Surg.*, vol. 101, no. 9, pp. 1063–1076, 2014.

[3] K. E. Roberts, R. L. Bell, and A. J. Duffy, "Evolution of surgical skills training," *World J. gastroenterol.: WJG*, vol. 12, no. 20, 2006, Art. no. 3219.

[4] S. S. Y. Tan and S. K. Sarker, "Simulation in surgery: A review," *Scottish Med. J.*, vol. 56, no. 2, pp. 104–109, 2011.

[5] K. Rangarajan, H. Davis, and P. H. Pucher, "Systematic review of virtual haptics in surgical simulation: A valid educational tool," *J. Surg. Educ.*, vol. 77, no. 2, pp. 337–347, 2020.

[6] S. G. Izard et al., "Virtual reality as an educational and training tool for medicine," *J. Med. Syst.*, vol. 42, no. 3, pp. 1–5, 2018.

[7] S. Condino et al., "How to build a patient-specific hybrid simulator for orthopaedic open surgery: Benefits and limits of mixed-reality using the microsoft hololens," *J. Healthcare Eng.*, vol. 2018, pp. 1–12, 2018.

[8] R. M. Viglialoro et al., "Augmented reality to improve surgical simulation: Lessons learned towards the design of a hybrid laparoscopic simulator for cholecystectomy," *IEEE Trans. Biomed. Eng.*, vol. 66, no. 7, pp. 2091–2104, Jul. 2019.

[9] M. Gmeiner et al., "Virtual cerebral aneurysm clipping with real-time haptic force feedback in neurosurgical education," *World Neurosurgery*, vol. 112, pp. e313–e323, 2018.

[10] S. Delorme et al., "Neurotouch: A physics-based virtual simulator for cranial microneurosurgery training," *Operative Neurosurgery*, vol. 71, no. suppl_1, pp. ons32–ons42, 2012.

[11] M. Hollensteiner, D. Fuerst, and A. Schrempf, "Artificial vertebrae for a novel simulator in minimally invasive spine surgery," *Biomed. Eng./Biomedizinische Technik*, vol. 58, no. SI-1-Track-R, 2013, Art. no. 000010151520134409.

[12] M. Takeuchi et al., "Multilayered artificial dura-mater models for a minimally invasive brain surgery simulator," *Appl. Sci.*, vol. 10, no. 24, 2020, Art. no. 9000.

[13] X. Wang et al., "Skin simulators for dermatological procedures," *Dermatol. Online J.*, vol. 21, no. 11, pp. 1–10, 2015.

[14] D. Fuerst, M. Hollensteiner, and A. Schrempf, "Assessment parameters for a novel simulator in minimally invasive spine surgery," in *Proc. 37th Annu. Int. Conf. IEEE Eng. Med. Biol. Soc.*, 2015, pp. 5110–5113.

[15] B. Esterer et al., "Development of artificial tissue-like structures for a hybrid epidural anesthesia simulator," in *Proc. 38th Annu. Int. Conf. IEEE Eng. Med. Biol. Soc.*, 2016, pp. 2099–2102.

[16] Q. Lin et al., "Development and validation of a near-infrared optical system for tracking surgical instruments," *J. Med. Syst.*, vol. 40, no. 4, pp. 1–14, 2016.

[17] Z. Zhou et al., "Optical surgical instrument tracking system based on the principle of stereo vision," *J. Biomed. Opt.*, vol. 22, no. 6, 2017, Art. no. 065005.

[18] A. M. Franz et al., "Electromagnetic tracking in medicine–A review of technology, validation, and applications," *IEEE Trans. Med. Imag.*, vol. 33, no. 8, pp. 1702–1725, Aug. 2014.

[19] G. Foerster et al., "Pre-clinical evaluation of a minimally invasive laryngeal pacemaker system in mini-pig," *Eur. Arch. Oto-Rhino- Laryngol.*, vol. 273, no. 1, pp. 151–158, 2016.

[20] A. H. Mueller et al., "Laryngeal pacing via an implantable stimulator for the rehabilitation of subjects suffering from bilateral vocal fold paralysis: A prospective first-in-human study," *Laryngoscope*, vol. 126, no. 8, pp. 1810–1816, 2016.

[21] C. Sittel and O. Guntinas-Lichius, *Neurolaryngology*. Berlin/Heidelberg, Germany: Springer, 2018, pp. 173–184.

[22] P. D. Parchi et al., "Patients specific spine simulators for surgical training and rehearsal in pedicle screws placement: A new way for surgical education," in *Proc. CAOS 20th Annu. Meeting Int. Soc. Comput. Assist. Orthopaedic Surg.*, 2020, vol. 4, pp. 225–230.

[23] D. Palmer et al., "A high-fidelity surgical model and perfusion simulator used to demonstrate ECMO cannulation, initiation, and stabilization," *J. Extra-Corporeal Technol.*, vol. 51, no. 2, pp. 94–99, 2019.

[24] C. Buschmann et al., "Mortui vivos docent," *Der Anaesthesist*, vol. 65, no. 8, pp. 601–608, 2016.

[25] W. M. Association et al., "World medical association declaration of Helsinki: Ethical principles for medical research involving human subjects," *Jama*, vol. 310, no. 20, pp. 2191–2194, 2013.

[26] A. Changoor et al., "Effects of refrigeration and freezing on the electromechanical and biomechanical properties of articular cartilage," *J. Biomechanical Eng.*, vol. 132, no. 6, 2010, Art. no. 064502.

[27] A. I. Medalia, "Electrical conduction in carbon black composites," *Rubber Chem. Technol.*, vol. 59, no. 3, pp. 432–454, 1986.

[28] P. Song, J. Song, and Y. Zhang, "Stretchable conductor based on carbon nanotube/carbon black silicone rubber nanocomposites with highly mechanical, electrical properties and strain sensitivity," *Composites Part B: Eng.*, vol. 191, 2020, Art. no. 107979.

[29] S. Basan and E. Sancaktar, "Electrical conductivity of carbon black-silicon rubber nanocomposites: Effects of strain, load and loading rate," *Curr. Nanomater.*, vol. 1, no. 3, pp. 195–200, 2016.

[30] H. Le et al., "Macro-and microdispersion of carbon black in liquid silicone rubbers," *Plast., Rubber Composites*, vol. 37, no. 8, pp. 367–375, 2008.

[31] B. Esterer et al., "A hybrid, low-cost tissue-like epidural needle insertion simulator," in *Proc. 39th Annu. Int. Conf. IEEE Eng. Med. Biol. Soc.*, 2017, pp. 42–45.

[32] H. Wu et al., "New tactile sensor for position detection based on distributed planar electric field," *Sensors Actuators A: Phys.*, vol. 242, pp. 146–161, 2016.

[33] H. Wu et al., "A flexible annular sectorial sensor for detecting contact position based on constant electric field," *Micromachines*, vol. 9, no. 6, 2018, Art. no. 309.

[34] J. O'Neill et al., "Stretchable, flexible, scalable smart skin sensors for robotic position and force estimation," *Sensors*, vol. 18, no. 4, 2018, Art. no. 953.

[35] MATLAB version 9.12.0.1927505 (R2022a), The Mathworks, Inc., Natick, Massachusetts, USA, 2022.

[36] S. Shenogin, L. Ferguson, and A. K. Roy, "The effect of contact resistance on electrical conductivity in filled elastomer materials," *Polymer*, vol. 198, 2020, Art. no. 122502.

[37] G. Foerster et al., "Electromyography of the posterior cricoarytenoid muscles: A consensus guideline," *Eur. Arch. Oto-Rhino- Laryngol.*, 279, pp. 3785–3793, 2022.